Journal of Nanobiotechnology

RESEARCH Open Access

Multifunctional glycyrrhizic acid-loaded nanoplatform combining ferroptosis induction and HMGB1 blockade for enhanced tumor immunotherapy

Xuan Sha[1†], Chuanbing Wang[1†], Yang Liu[1†], Nan Zhong[1], Yishi Lu[1], Qi Zhang[2], Shangyu Lu[3], Doudou He[1], Yingying Jin[1], Yuxia Tang[1*] and Shouju Wang[1*]

Abstract

Inducing ferroptotic cell death has been recognized as a promising approach in cancer therapy. However, ferroptosis can provoke tumor infiltration by myeloid-derived suppressor cells (MDSCs) through HMGB1 secretion, causing a tumor suppressive immune response. On the other hand, ferroptosis also occurs the immune cells due to its non-selective properties, which can compromise anti-tumor immunity. To address these challenges, a two-pronged approach is proposed, encompassing selectively triggered ferroptosis in tumor cells and HMGB1 blockade, aimed at eliciting systemic anti-tumor immunity and alleviating immunosuppression. Herein, GSH-specific driven nanoplatform is composed of uniform FeOOH nanospindles coated with tetrasulfide bond-bridged mesoporous organosilica (DMOS) shell, and loaded with the HMGB1 inhibitor, glycyrrhizic acid (GA). This nanoplatform is endowed with high glutathione (GSH) depletion efficiency and exhibits highly efficient Fe^{2+} and ROS generation capacity, which promotes the accumulation of LPO and subsequently induces ferroptosis. Concurrently, the inhibition of HMGB1 release counteracts the immunosuppressive effects within the tumor microenvironment. This innovative nanoplatform effectively suppresses the growth of 4T1 tumors and notably enhancing the therapeutic outcomes of immune checkpoint blockade across experimental data. The collective findings indicate its potential as a reliable therapeutic strategy for boosting ferroptosis-mediated tumor immunity with favorable safety profiles.

Introduction

Cancer immunotherapy has gained substantial attention as a revolutionary systemic treatment strategy [1, 2]. However, its therapeutic efficacy in most solid tumors is significantly hampered by a relatively low response rate, which is predominantly due to the suppressive tumor immune microenvironment [3, 4]. Ferroptosis, a form of iron-dependent regulated cell death, driven by the accumulation of lipid peroxides on cellular membranes, has recently been identified as a crucial regulator within the tumor immune microenvironment [5]. Considerable evidence indicates that ferroptosis not only restricts tumor

†Xuan Sha, Chuanbing Wang and Yang Liu contributed equally to this work.

*Correspondence:
Yuxia Tang
tangyuxia5@163.com
Shouju Wang
wangshouju@njmu.edu.cn

Full list of author information is available at the end of the article

Graphical abstract

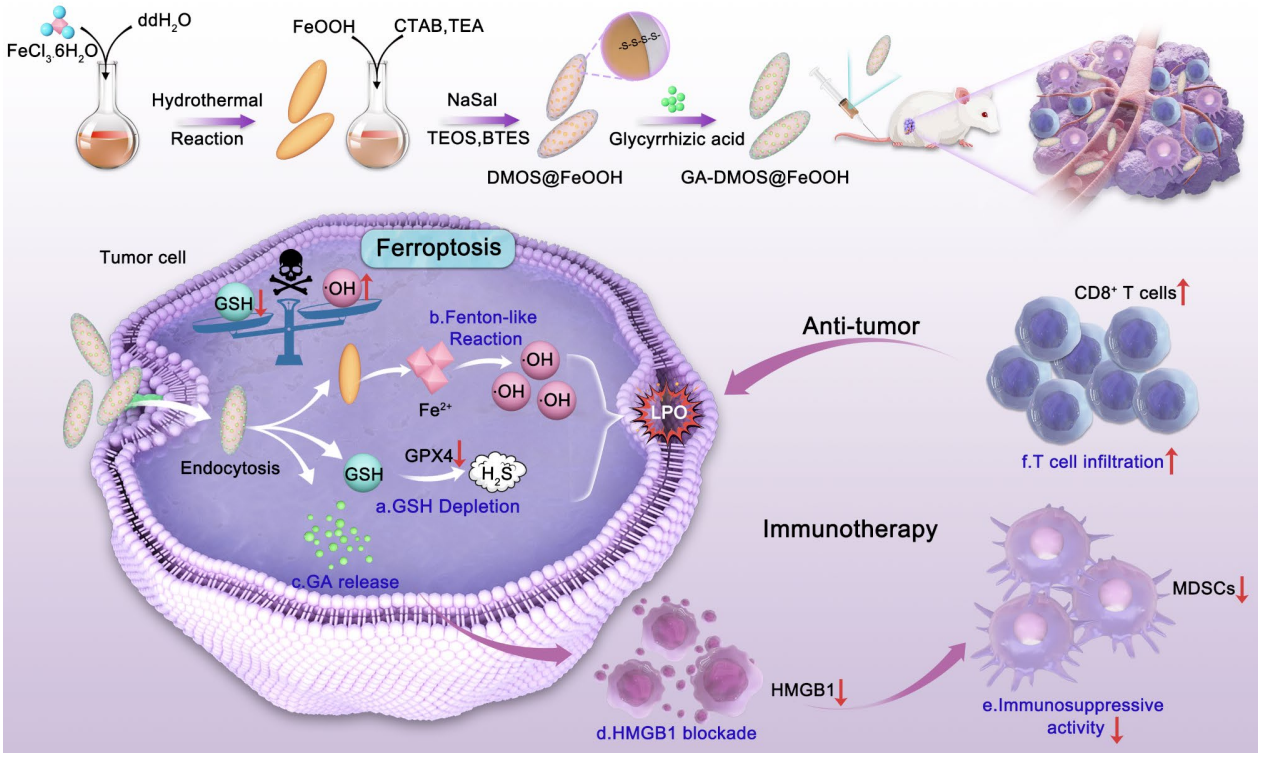

Keywords Ferroptosis, Immunotherapy, Nanomedicine, GSH depletion, HMGB1 blockade

growth by inducing cell death but also exhibits potential in augmenting immunotherapy responses [6–9].

Notably, ferroptosis plays a complex role in modulating the tumor immune microenvironment [10]. It can eliminate tumor cells and enhance immunotherapy outcomes, yet it also induces the release of high mobility group box 1 (HMGB1) from dying tumor cells [11]. HMGB1 functions as a potent recruiter of myeloid-derived suppressor cells (MDSCs), which subsequently suppress the local immune microenvironment and counteract the activation of immune cells mediated by ferroptosis [12]. Claire Conche et al. have demonstrated that by neutralizing HMGB1 during ferroptosis induction, the sensitivity of primary and metastatic liver cancers to immune checkpoint inhibitors can be improved [13, 14]. Therefore, the combination of ferroptosis induction and HMGB1 blockade is essential for maximizing the pro-immunotherapeutic potential of ferroptosis.

Another limiting factor in activating the tumor microenvironment through ferroptosis is that it simultaneously triggers the death of immune cells while inducing tumor cell death [15, 16]. Thus, the development of tumor cell-specific ferroptosis inducers is crucial for optimizing the efficacy of subsequent immunotherapy [17]. The majority of tumor cells possess an elevated level of intracellular glutathione (GSH) [18, 19]. GSH, with its strong reducing capacity, impairs the effectiveness of ferroptosis-based therapies by neutralizing lipid peroxides and inhibiting the accumulation of lipid reactive oxygen species (ROS) [20, 21]. Therefore, the design of GSH-activated ferroptosis inducers can avoid ferroptosis-induced damage to immune cells and deplete GSH in tumors to enhance the therapeutic potency of ferroptosis.

In view of the above, in this study, we propose a GSH-triggered ferroptosis-inducing nanoplatform with HMGB1 blockade functionality. Specifically, this engineered nanoplatform consists of uniform FeOOH nanospindles coated with tetrasulfide bond-modified mesoporous organosilica (DMOS) shells and loaded with the HMGB1 inhibitor, glycyrrhizic acid (GA). The DMOS shells can suppress the ferroptosis-inducing ability of FeOOH nanospindles in a low GSH environment, preventing damage to normal immune cells. In contrast, in the tumor cell-specific high GSH environment, the tetrasulfide bonds are reductively cleaved, activating the ferroptosis-inducing capacity of FeOOH nanospindles, thereby killing tumor cells and activating the immune system. Concurrently, GA is released in response,

inhibiting HMGB1 release and synergistically activating the immune microenvironment.

Owing to the reaction between the tetrasulfide bond-modified mesoporous organosilica and GSH [22], this nanoplatform selectively induces ferroptosis in cancer cells without sparing immune cells. We have comprehensively elucidated the mechanistic underpinnings of GA-DMOS@FeOOH-mediated ferroptosis and evaluated the efficacy and safety of GA-DMOS@FeOOH nanoparticles in enhancing tumor immunotherapy.

Materials and methods

Synthesis of FeOOH nanospindles

FeOOH nanospindles were preparaed via a hydrothermal method based on previous literature [23]. Briefly, 0.68 g of $FeCl_3{\cdot}6H_2O$ was first dissolved in 50 mL of deionized water to create a homogeneous solution. Then keep stirring vigorously at 80 °C until the solution became cloudy. The resulting products were centrifugated at 8,000 rpm for 30 min, washed multiple times with deionized water, and finally redispersed in deionized water for subsequent use.

Synthesis of FeOOH nanospindles coated with tetrasulfide bond incorporated mesoporous organosilica (DMOS@FeOOH NPs)

DMOS@FeOOH nanoparticles (NPs) were synthesized following a procedure outlined in previous reports [24]. In brief, 61 μL of TEA was dissolved in 25 mL of deionized water and keep stirring slowly. Next, 20 mg of FeOOH, 160 mg of CTAB, 64 mg of NaSal were added to the mixture and stirred for an additional 2 h. A mixture of TEOS and BTES was added slowly to the solution drop by drop, which was kept strring at 80 °C for 12 h. The reaction solution was centrifugated and washed with ethanol. This dispersion was dissolved in ethanol and kept stirred for 6 h. This washing process need to be repeat multiple times to ensure complete template removal.

Synthesis of DMOS@FeOOH loaded with GA NPs

For glycyrrhizic acid loading, the GA solution was added to DMOS@FeOOH NPs and stirred overnight to acquire GA-DMOS@FeOOH NPs. After reaction finished, the products were collected by centrifugation to remove any unincorporated glycyrrhizic acid. The glycyrrhizic acid concentration was determined through NanoDrop, based on its absorbance at 253 nm. The glycyrrhizic acid loading efficiency (LE) and encapsulation efficiency (EE) were respectively calculated using the following equations:

$$\text{Loading Efficiency (LE)} = \frac{m_{GA,\,total} - m_{GA,\,free}}{m_{DMOS@FeOOH}} \times 100\%$$

$$\text{Encapsulation Efficiency (EE)} = \frac{m_{GA,\,total} - m_{GA,\,free}}{m_{GA,\,total}} \times 100\%$$

GSH depletion

Different nanoparticles were incubated with GSH solution. For time-dependent studies, DMOS@FeOOH NPs were exposed to varying GSH concentrations over different time intervals. DTNB solution was added and incubated at 25 °C after the mixture were centrifugated and the absorbance at 412 nm was recorded to determine the GSH consumption through UV-Vis spectroscopy.

H_2S generation in vitro

To quantify H_2S production, different nanoparticles were dispersed in a 10 mM GSH aqueous solution and stirred for various time intervals. After centrifugation, the supernatants were collected and incubated with a mixture solution of zinc acetate/sodium acetate in a mass ratio of 4:1. Methylene blue was then generated by the addition of DMPD·2HCl and $FeCl_3$. The absorbance at 664 nm was detected after incubation. H_2S generation was measured through standard curve derived from Na_2S. For visual observation of H_2S production, DMOS@FeOOH NPs were mixed with GSH solution. A circular piece of filter paper saturated with $Pb(NO_3)_2$ solution was placed over the bottle opening. The reaction mixture was stirred for varying time intervals, and the color change was monitored as an indicator of H_2S production.

GA released from GA-DMOS@FeOOH NPs

To investigate the release of glycyrrhizic acid, GA-DMOS@FeOOH NPs were mixed with GSH solution at various concentrations. The mixture was stirred for different time intervals. The release profile of GA was evaluated by detecting the absorbance at 253 nm after centrifugation at each sampling interval.

Fe2+ detection and generation of •OH in vitro

Fe^{2+} concentration was performed through 1,10-phenanthroline serving as a chelating agent. Various nanoparticles were incubated with 10 mM GSH solution at pH 5.0. Meanwhile, DMOS@FeOOH NPs were also dispersed in GSH solutions at different pH values for different time points. After centrifugation at 13,500 rpm, the supernatants were mixed with 15% 1,10-phenanthroline, and then the absorbance at 510 nm was recorded.

To asses the generation of •OH induced by DMOS@FeOOH through Fenton-like reaction, the supernatants were reacted with hydrogen peroxide (H_2O_2), and TMB solution in dimethyl sulfoxide was added. The formation of •OH was quantified by absorbance measurement at 652 nm. Additionally, DMOS@FeOOH were dissolved in GSH solution under different pH conditions for various time points to detect the production of •OH. Absorbance at 652 nm was recorded as an indicator of •OH formation.

In vitro cytotoxicity

MTT assays were performed to assess nanoparticle toxicity in 4T1 and 3T3 cells. After overnight culture in 96-well plates, cells were exposed to fresh medium containing various nanoparticle concentrations for additional 24 h. Afterward, MTT reagent was introduced and the cells were maintained at 37 °C for 4 h without light exposure. Formazan crystals were solubilized through DMSO and optical density were quantified at 490 nm through microplate spectrophotometer.

Live/Dead cell staining: To further visually observe cytotoxicity, after different nanoparticles exposure, 4T1 cells were stained with Calcein AM and PI solution for 30 min. Then the viability of cells were visualized through fluorescence microscopy.

Intracellular GSH-consumption

After overnight culture in 6-well plates, 4T1 and 3T3 cells were treated with different nanoformulations for another 12 h: (1) Control; (2) FeOOH; (3) DMOS@FeOOH; (4) GA-DMOS@FeOOH. Following PBS washing, cells were treated with Thiol Tracker Violet staining solution (10 μM) for 30 min. After removal of the staining solution, cells underwent PBS washes to eliminate unbound dye. Fluorescence images were captured to visualize intracellular GSH consumption.

Intracellular H2S generation, Fe2+ detection and ROS production

After overnight culture in 6-well plates, 4T1 cells were exposed to different nanoformulations. After removing residual nanoparticles, the cells were incubated with the following fluorescence probes: WSP-5 solution (50 μM) for H_2S detection, FeRhoNox-1 (10 μM) for Fe^{2+} generation, and DCFH-DA (10 μM) for ROS production. Fluorescence images were captured to assess intracellular H_2S generation, Fe^{2+} levels, and ROS production.

Investigation of the ferroptosis pathway

The ferroptosis pathway was investigated by examining the expression level of GPX4 and the cystine transporter SLC7A11 using Western blotting. Briefly, following nanoparticle treatment, 4T1 cells were lysed in RIPA buffer. Samples were separated by SDS-PAGE, transferred to polyvinylidene fluoride (PVDF) membranes and probed with primary antibodies (GPX4, SLC7A11, β-actin) at 4 °C overnight. After secondary antibody incubation, protein bands were exposed to ECL chemiluminescence solution for quantitative analysis.

For intracellular lipid peroxide (LPO) detection, after different treatments, 4T1 cells were stained with $BODIPY^{581/591}$-C11 (10 μM) probe. After washing with PBS, the cells was observed by fluorescence, which were excited with 488 nm and 581 nm lasers to detect lipid peroxides, respectively.

For mitochondrial integrity assessment, after different treatments, 4T1 cells were stained with MitoTracker Red solution (500 nM) for 45 min and observed through fluorescence. Furthermore, JC-1 probe was also applied to detect the mitochondrial integrity. After various treatments, cells were incubated with JC-1 working solution for 20 min. JC-1 monomer and aggregate forms were detected under excitation at 485 nm with emissions measured at 530 nm (green) and 590 nm (red), respectively.

In vitro HMGB1 localization measurement

HMGB1 localization was evaluated through immunofluorescence analysis. After fixing, permeabilizing and blocking, 4T1 cells were incubated with anti-HMGB1 antibody overnight, then exposed to AF488-conjugated secondary antibody and DAPI for fluorescence imaging.

Extracellular release of HMGB1 was quantitatively assessed through HMGB1 ELISA Kit (Elabscience, China). After different treatments, the supernatant was centrifugated at 12,000 rpm. Then HMGB1 levels in the supernatant were measured according to the manufacturer's protocol.

In vivo anti-tumor effect evaluation

To establish 4T1 mammary model, 4T1 (5×10^5) cells were subcutaneously inoculated into the right dorsal flank of female Balb/c mice (15–18 g, 6–8 weeks). Once the tumor volume reached approximately 50 mm^3, the tumor-bearing mice were randomly divided into six groups ($n = 8$) for treatment via intravenous injection as follows: (1) Control, (2) FeOOH, (3) DMOS@FeOOH, (4) GA-DMOS@FeOOH, (5) ICB, (6) ICB + GA-DMOS@FeOOH (combined therapy). For ICB therapy, mice were administered intraperitoneal injections of αPD-L1 antibody. Tumor volume and body weight were recorded every two days. Tumor volume was calculated using the formula: [(length × $width^2$)/2]. After 14 days of treatment, mice were sacrificed, and tumors were collected for histological analysis. Immunohistochemical assays, including KI67, TUNEL, ROS, HMGB1, GPX4, SLC7A11, and LPO, were performed on tumor sections to evaluate the in vivo antitumor efficacy of GA-DMOS@FeOOH.

Flow cytometry analysis of the tumor microenvironment

Immune cell profiling in tumor and spleen tissues was performed by flow cytometry. Single-cell suspensions were prepared through enzymatic digestion (collagenase IV/DNase I), filtration, and counting. Cells were stained with Fixable Viability Dye, blocked with anti-CD16/32, and incubated with antibody cocktails. For MDSCs analysis in tumors, the following antibodies were used: anti-CD45-FITC, anti-CD11b-BV605, anti-Gr-1-PE-Cy7,

anti-Ly6G-PE, and anti-Ly6C-APC. T cell infiltration in tumors was analyzed using anti-CD45-AF700, anti-CD3-Percp-Cy5.5, anti-CD4-PE-Cy5.5, and anti-CD8-PE antibodies.

Spleen samples were mechanically dissociated in RPMI 1640 medium, followed by centrifugation. Erythrocytes were lysed using cold lysis buffer, and the reaction was terminated with PBS before filtration. The staining procedure was performed as described above for tumor samples.

Biosafety evaluation

Hemolysis assay

The blood compatibility of GA-DMOS@FeOOH was evaluated through hemolysis assay. RBCs isolated from Balb/c mice blood were mixed with GA-DMOS@FeOOH at different concentrations (200 μL RBCs: 800 μL sample). Deionized water and saline served as positive and negative controls, respectively. After incubation and centrifugation, hemolysis rates were determined by measuring supernatant absorbance at 541 nm and calculated using the following formula:

$$\text{Hemolysis } (\%) = \frac{\text{OD}_{\text{sample}} - \text{OD}_{\text{negative control}}}{\text{OD}_{\text{positive control}} - \text{OD}_{\text{negative control}}} \times 100\%$$

In vivo biocompatibility assessment

Balb/c mice ($n = 3$) received intravenous GA-DMOS@FeOOH injections on days 0, 7, 14, and 21. At termination, blood was collected for hematological and biochemical analyses, while major organs were processed for hematoxylin and eosin staining.

Statistical analysis

All data are expressed as the mean ± standard deviation (SD). Comparisons between multiple groups were performed using one-way analysis of variance (ANOVA), while differences between two groups were assessed with a Student's t-test. Statistical significance was determined at the following thresholds: $^{*}p < 0.05$, $^{**}p < 0.01$, and $^{***}p < 0.001$.

Results

Physiochemical properties of GA-DMOS@FeOOH nanoparticles

As illustrated in Scheme 1, DMOS@FeOOH nanoparticles were preparaed through a two-step approach. Initially, FeOOH nuclei were formed through the hydrolysis of Fe^{3+}, followed by the oriented self-assembly of the particles into a spindle-like morphology [25]. The TEM image of the as-synthesized FeOOH NSs in Fig. 1a shows a uniform distribution of particles with dimensions of approximately 36.90 × 146.22 nm. In the next

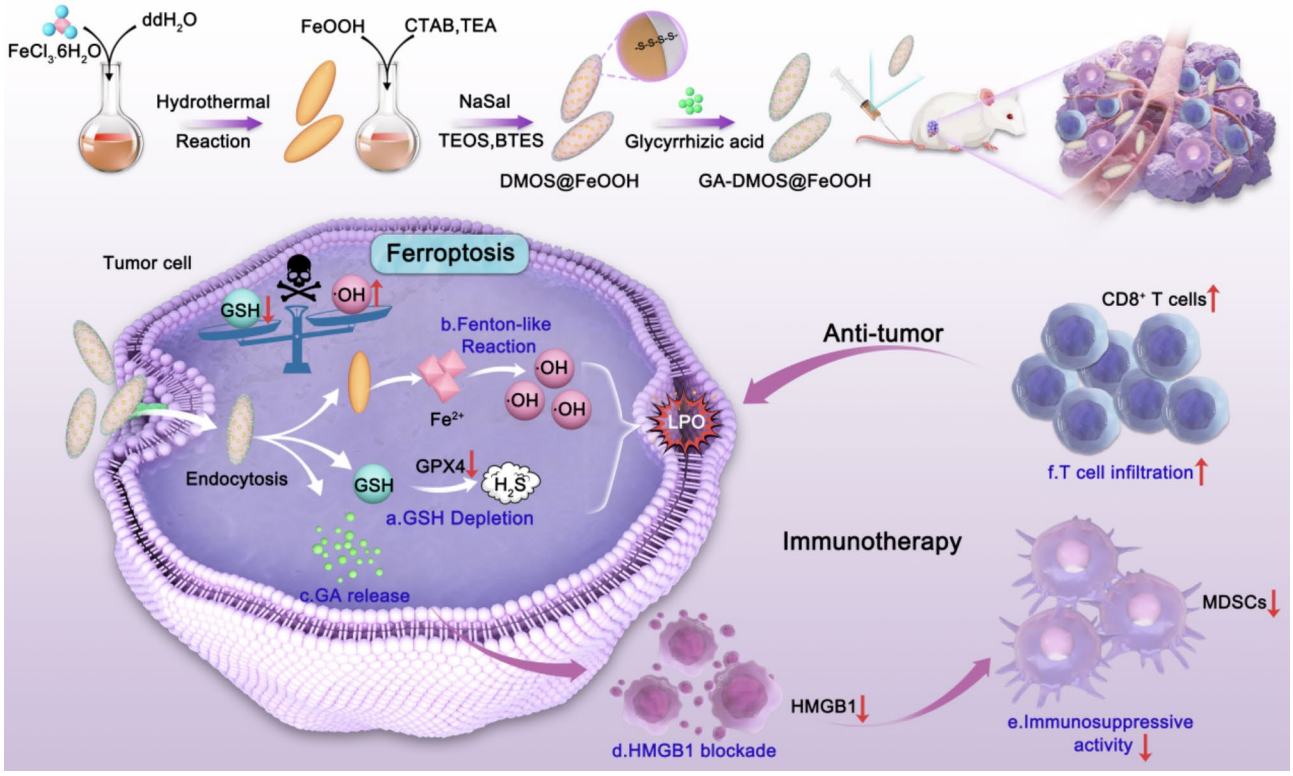

Scheme 1 Schematic illustration of GA-DMOS@FeOOH nanoplatform-induced ferroptosis to enhance tumor immunotherapy

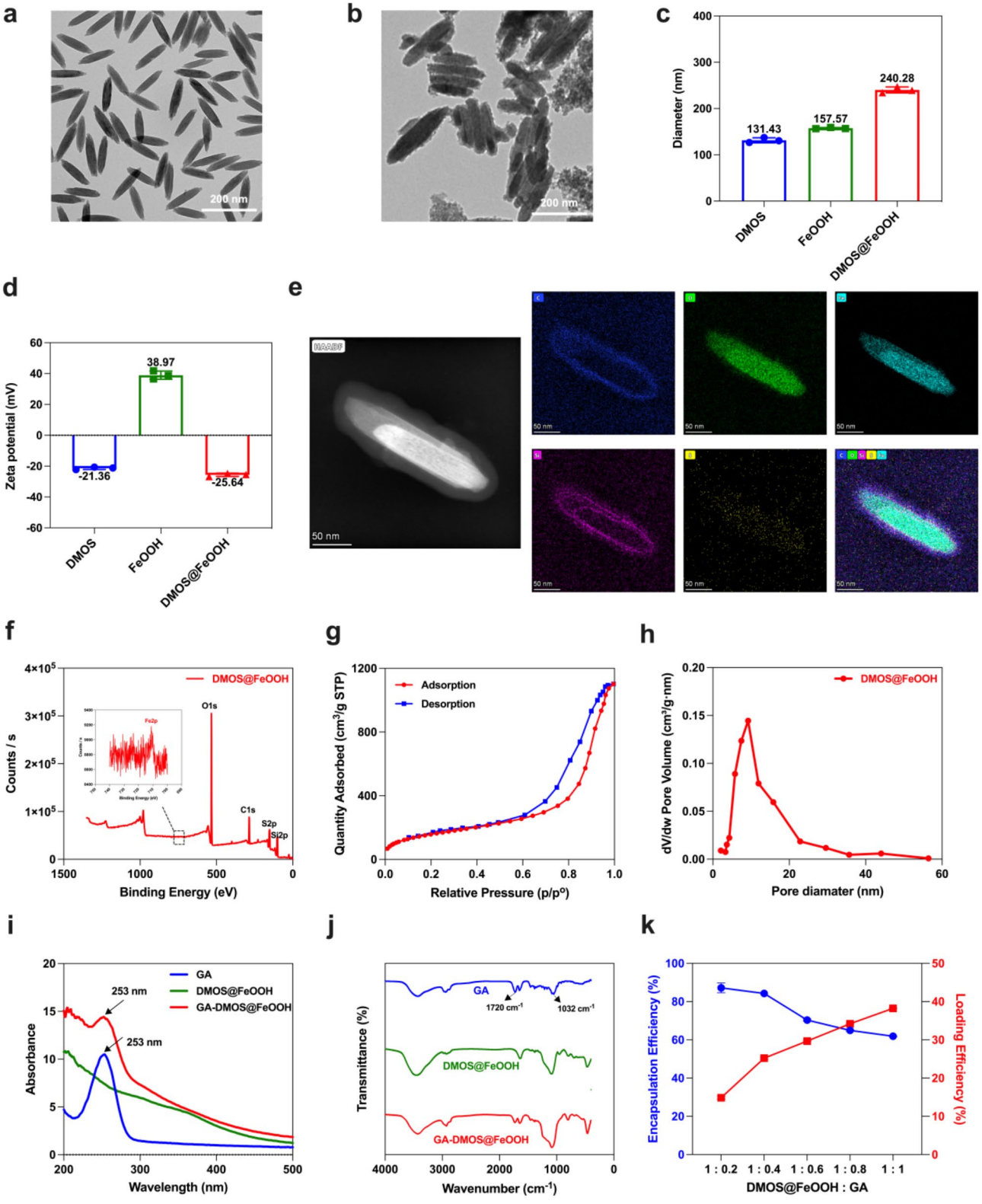

Fig. 1 Characterization of GA-DMOS@FeOOH NPs. TEM images of (**a**) FeOOH and (**b**) DMOS@FeOOH NPs. (**c**) Hydrodynamic diameter and (**d**) Zeta potential of different NPs detected by DLS ($n = 3$). (**e**) HAADF-STEM images with Elemental mapping patterns of DMOS@FeOOH NPs. (**f**) XPS spectrum of DMOS@FeOOH NPs. (**g**) N_2 adsorption and desorption isotherm and (**h**) pore size distribution of DMOS@FeOOH NPs. (**i**) UV-Vis spectra and (**j**) FTIR spectra of different NPs. (**k**) Loading efficiency and encapsulation efficiency of GA by DMOS@FeOOH NPs

step, inspired by the synthesis of mesoporous organosilica nanoparticles (Figure S1), FeOOH NSs were surface-coated with tetrasulfide-bond-incorporating silica. This process was achieved by TEOS and BTES in the presence of CTAB and NaSal [26]. The TEM image shown in Fig. 1b reveals that the DMOS shell uniformly coated the FeOOH nanospindles, resulting in a core@shell structure. After coating, the average hydrodynamic diameter of the DMOS@FeOOH NPs increased to 240.28 ± 6.37 nm (Fig. 1c). This increase in size is indicative of the successful coating of DMOS. Additionally, the zeta potential also shifted from 38.97 ± 2.68 mV for bare FeOOH to − 25.64 ± 1.08 mV for the DMOS@FeOOH (Fig. 1d), further confirming the formation of the DMOS shell. To further validate the structure of DMOS@FeOOH, high resolution TEM and EDS mapping were performed (Fig. 1e). The C, Si, and S elements were localized predominantly within the outer shell, while Fe was confined to the nanocore. The O element, however, showed a uniform distribution throughout the entire nanoplatform, indicating the successful fabrication of DMOS@FeOOH nanoparticles. XPS analysis of DMOS@FeOOH (Fig. 1f) revealed the presence of C, O, Fe, Si, S elements, validating the successful incorporation of the tetrasulfide bonds in the shell. The XPS spectra of relevant elements in DMOS@FeOOH nanoparticles are displayed in Figure S2, further confirming the successful tetrasulfide bond loading. The XRD pattern of DMOS@FeOOH NPs (Figure S3) exhibited diffraction peaks that correspond to the standard FeOOH NSs (JCPDS No. 34-1266), confirming the crystalline nature of the nanospindles.

To gain insights into the surface pore structure of DMOS@FeOOH NPs, the nitrogen adsorption-desorption isotherm was analyzed. The isotherm displayed characteristic type IV behavior (Fig. 1g), indicative of mesoporous materials. The BET surface area was calculated to be 584.4636 m^2/g, with a uniform mesopore size of 11.58 nm (Fig. 1h). This suggests that DMOS@FeOOH nanoparticles possess a significant drug-loading capacity due to their mesoporous structure. Next, UV-Vis absorption spectra of GA-DMOS@FeOOH nanoparticles showed a prominent absorption peak around 253 nm, which corresponds to the characteristic absorption of GA. This peak remained intact in the GA-DMOS@FeOOH NPs, as shown in Fig. 1i, indicating the successful loading of GA. Meanwhile, FTIR spectroscopy further confirmed the successful incorporation of GA into the DMOS@FeOOH nanoparticles. The sharp peak around 1720 cm^{-1} (Fig. 1j) corresponds to the carbonyl stretching vibration of GA, while the broad peak near 1032 cm^{-1} originated from C-O stretching vibration in the dextran portion of the DMOS shell. Finally, to optimize the drug-loading delivery system, the molar ratio of GA to DMOS@FeOOH was altered. The optimal ratio was determined to be 1:0.4 (DMOS@FeOOH: GA) for subsequent experiments (Fig. 1k). A standard curve for GA was also established through UV-Vis spectra (Figure S4).

In addition, the stability of GA-DMOS@FeOOH NPs in serum was evaluated by tracking changes in diameter and polydispersion index over time. DLS analysis revealed that the diameter of GA-DMOS@FeOOH remained nearly unchanged over a span of 7 days (Figure S5). And the polydispersion index remained consistently about 0.2, indicating a narrow size distribution and stable colloidal dispersion. These results suggest that GA-DMOS@FeOOH nanoparticles maintain excellent stability in serum, which is essential for their sustained performance and potential therapeutic efficacy in biological systems.

Capability of GSH depletion, H2S release, drug release, Fe2+ generation and •OH production

Due to the high sensitivity of tetrasulfide bonds to reductive environments, the DMOS@FeOOH incorporating these bonds are able to deplete GSH [27], realizing an effective Fe^{2+}-mediated multistep reaction (Fig. 2a). DTNB probe was acquired to judge the feasibility of utilizing DMOS@FeOOH in depleting GSH, based on the specific chemical reaction between DTNB and thiol groups, generating TNB with a distinct absorption maximum at 412 nm. As depicted in Fig. 2b, the characteristic absorbance peak at 412 nm presented a drop tendency in the presence of tetrasulfide bonds in DMOS NPs, demonstrating the efficient glutathione-scavenging properties of DMOS@FeOOH, suggesting its potential application in redox homeostasis modulation within biological systems.

Furthermore, the tetrasulfide-containing nanostructure demonstrates an additional GSH-responsive mechanism through H_2S generation. This gasotransmitter production occurs via a redox reaction between the tetrasulfide bond and intracellular glutathione, serving as an alternative evidence of GSH depletion capability. The H_2S generation efficiency of different nanoparticles was evaluated based on H_2S ELISA kit. Figure 2c illustrated that the time-dependent H_2S release after DMOS@FeOOH NPs incubated with GSH, highlighting their GSH-responsive H_2S generation. Meanwhile, Fig. 2d illustrates the use of $Pb(NO_3)_2$ test paper, which reacts with H_2S to produce a brown-black lead sulfide precipitate [28]. Over time, the test paper changed color from white to dark brown, confirming H_2S production by DMOS@FeOOH NPs.

Given the favorable GSH-responsive properties of nanoparticles, we next explored the drug release behavior of glycyrrhizic acid from GA-DMOS@FeOOH NPs. As shown in Fig. 2a, the release mechanism of glycyrrhizic acid is closely related to the cleavage of the tetrasulfide bonds. Tetrasulfide bonds are known to be susceptible to cleavage in the presence of high concentrations of

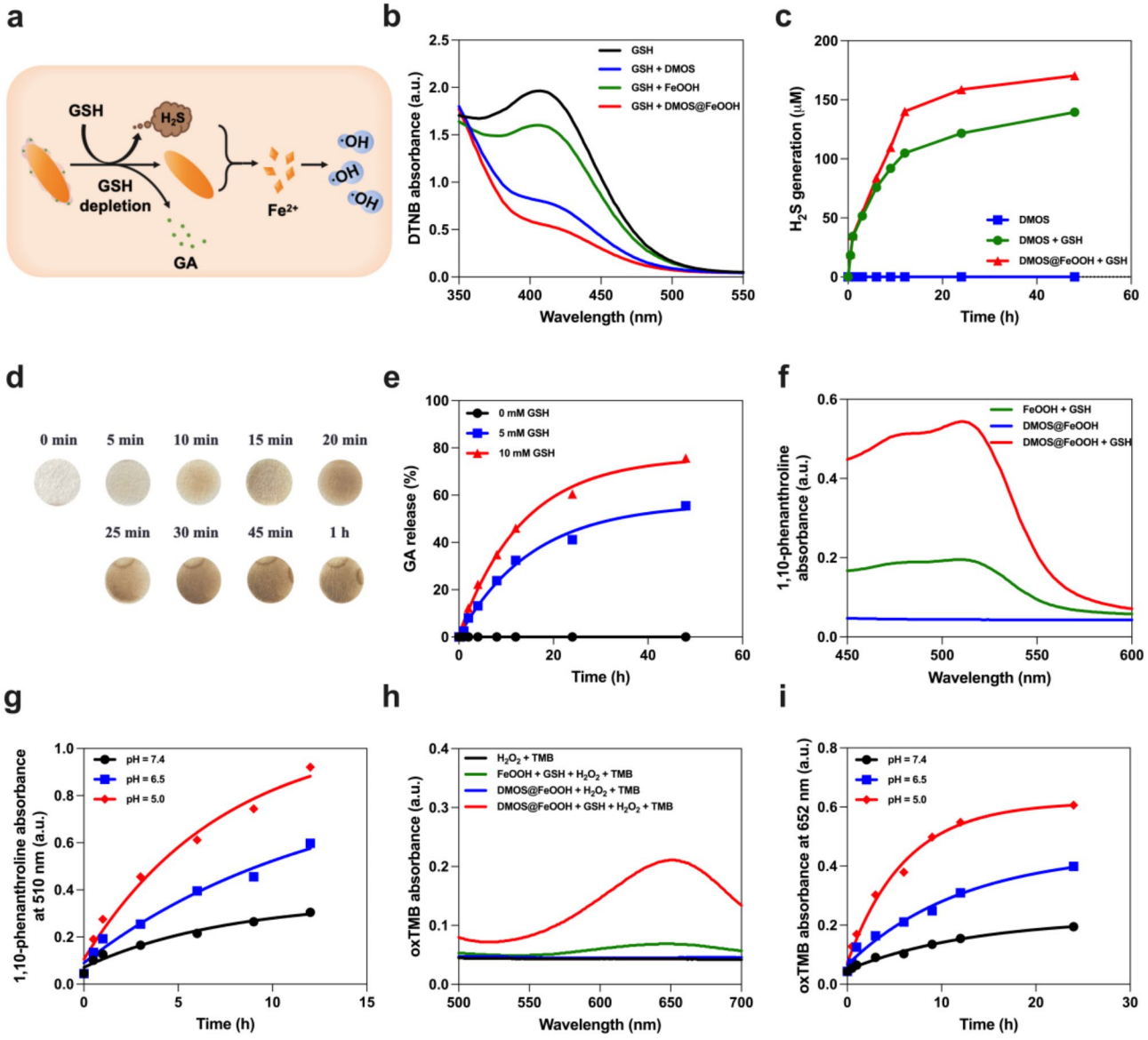

Fig. 2 GSH-activatable generation of Fe^{2+} and •OH. (**a**) Schematic illustration of the reaction mechanism of GA-DMOS@FeOOH in TME. (**b**) UV-vis spectra analysis of GSH depletion measured by DTNB probe. (**c**) H_2S generation from different nanoparticles examined by ELISA kit ($n = 3$). (**d**) Visual monitoring of H_2S production through lead nitrate paper assay. (**e**) GA release from GA-DMOS@FeOOH after treated with different concentrations of GSH ($n = 3$). (**f**) UV-vis absorption spectra of Fe^{2+} generation from different nanoparticles detected by 1,10-phenanthroline probe. (**g**) The Fe^{2+} release from DMOS@FeOOH NPs dispersed in GSH solutions with various pH values ($n = 3$). (**h**) UV-vis absorption spectra of •OH generation from different nanoparticles examined through TMB degradation. (**i**) Response of •OH generation from DMOS@FeOOH NPs under different pH conditions of GSH

reducing agents, such as GSH, which is abundant in the tumor microenvironment. GSH can readily react with the sulfur atoms in the tetrasulfide bond through its thiol group, leading to the breaking of the bond. This reaction causes structural changes in the DMOS shell, resulting in the release of the encapsulated glycyrrhizic acid. The GSH depletion ability and H_2S generation of DMOS@FeOOH NPs indirectly verified that the cleavage of tetrasulfide bonds, supporting this mechanism. The release kinetics of GA were investigated under varying GSH concentrations (0, 5 mM, and 10 mM). Figure 2e shows that GA release was most pronounced at 10 mM GSH, with the release rate being concentration-dependent. These findings demonstrate that the redox-responsive cleavage of tetrasulfide bonds mediated by GSH serves as a crucial mechanism for tumor-specific and controlled GA release, highlighting the potential of GA-DMOS@FeOOH nanoparticles as a GSH-responsive nanoplatform for targeted cancer therapy.

Simultaneously, FeOOH NSs could quickly interact and absorb H_2S to generate Fe^{2+} with the generation of H_2S. Fe^{2+} release was quantitatively analyzed using

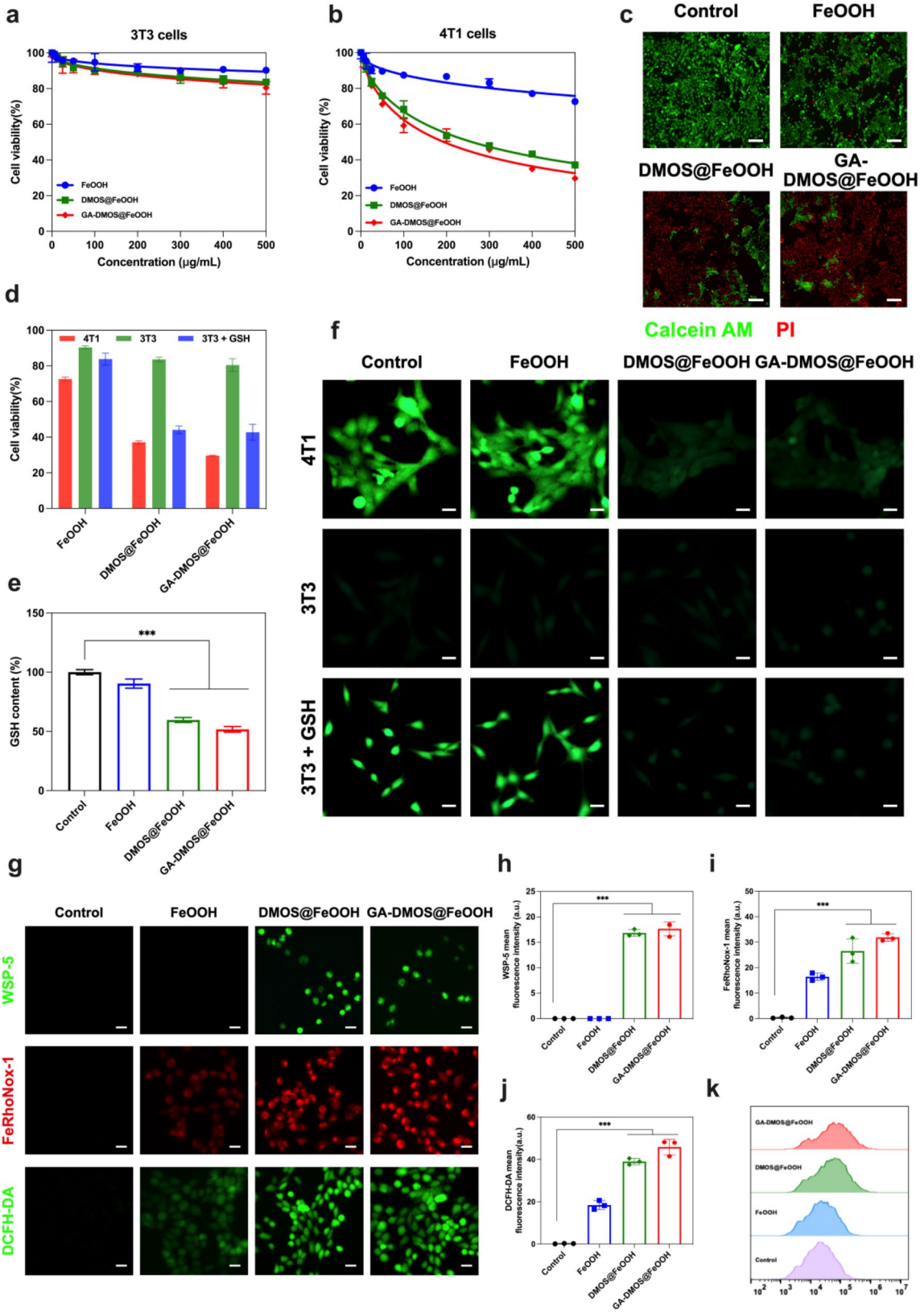

Fig. 3 (See legend on next page.)

(See figure on previous page.)

Fig. 3 Selectively cytotoxicity ability of DMOS@FeOOH NPs. Cell viability of (**a**) 3T3 and (**b**) 4T1 incubated with different nanoparticles at different concentrations. (**c**) Fluorescence images of Calcein-AM (green)/PI (red) co-stained 4T1 cells after different treatments (scalar bar: 100 μm). (**d**) Cytotoxicity of different nanoparticles in 3T3, 4T1 cells and 3T3 + GSH. (**e**) Intracellular concentration of GSH in 4T1 cells in different groups. (**f**) Intracellular GSH-depletion capability detected by ThiolTracker Violet GSH probe.(scalar bar: 50 μm). (**g**-**j**) Fluorescence images and corresponding quantitative analysis of WSP-5, FeRhoNox-1 and DCFH-DA probe (scalar bar: 50 μm). (**k**) Flow cytometry analysis of intracellular ROS contents after different treatments

1,10-phenanthroline, which forms a deep red complex with Fe^{2+}, detectable at 510 nm via UV-Vis. In the presence of DMOS shell, the absorbance of DMOS@FeOOH NPs at 510 nm increased after co-incubated with 10 mM GSH solution (Fig. 2f), which verified H_2S triggered the Fe^{2+} release. In Fig. 2g, we demonstrate the release behavior of Fe^{2+} under different pH conditions, showing that an acidic environment accelerates the release of Fe^{2+}, which can be explained through the chemical properties of FeOOH and the effect of acidic conditions on the reduction of Fe^{3+}. FeOOH nanoparticles consist of Fe^{3+} ions and hydrated oxide structures, which are relatively stable in neutral or basic environments. However, in acidic conditions, the higher concentration of H^+ ions could interact with the surface of FeOOH, facilitating the reduction of Fe^{3+} to Fe^{2+}. Therefore, acidic environments provide a favourable condition that promotes the release of Fe^{2+}, further enhancing the induction of ferroptosis in tumor cells.

To investigate Fe^{2+}-mediated •OH generation triggered by DMOS@FeOOH, TMB was used as an indicator. The •OH generation is catalyzed by Fe^{2+} through a Fenton-like reaction [29]. As depicted in Fig. 2h, time-dependent enhancement of TMB oxidation was observed at 652 nm in the presence of GSH-treated DMOS@FeOOH nanoparticles upon H_2O_2 addition, providing direct evidence of •OH production. Similarly, Fig. 2i demonstrates the continuous production of •OH from DMOS@FeOOH NPs under different pH conditions. The production rate of •OH was again slowest at pH 7.4 and highest at pH 5.0, in line with the acidic conditions typically found in tumors.

Taken together, these results strongly confirm the GSH-responsive properties of GA-DMOS@FeOOH NPs. They effectively deplete GSH within the tumor microenvironment (TME), generating Fe^{2+} and •OH in acidic conditions. This suggests that GA-DMOS@FeOOH NPs are a promising candidate for promoting ferroptosis in cancer therapy, leveraging both GSH depletion and ROS generation.

Selectively cytotoxicity of GA-DMOS@FeOOH NPs

The selectively cytotoxicity of different nanoparticles toward tumor cells and normal cells was investigated via MTT assay. Murine fibroblast cell line 3T3 cells were chosen as the normal cell model, while 4T1 murine breast cancer cells served as the tumor cell model. Figure 3a revealed that 3T3 cells maintained strong viability even when exposed to high concentrations of various nanomaterials, indicating the favorable biocompatibility of these nanoparticles. In contrast, 4T1 cells exhibited a significant reduction in viability when treated with DMOS@FeOOH NPs, which decreased to 37.12%. The viability further decreased to 29.62% for GA-DMOS@FeOOH NPs, highlighting the tumor-specific cytotoxicity of GA-DMOS@FeOOH NPs (Fig. 3b). To visually confirm the cytotoxic effects, live/dead cell differentiation was performed through Calcein-AM/PI double-staining assay. The fluorescence images revealed that GA-DMOS@FeOOH nanoparticles demonstrated superior tumor cell ablation efficiency, which correlated well with the quantitative viability data obtained from MTT assays (Fig. 3c). These results collectively support the hypothesis that GA-DMOS@FeOOH NPs preferentially target and kill tumor cells over normal cells.

Based on this phenomena, we initially investigated the cellular internalization efficiency of Cy5-DMOS@FeOOH NPs in both 3T3 and 4T1 cells. Results from CLSM and flow cytometry (FCM) analysis demonstrated comparable cellular uptake between 3T3 and 4T1 cells (Figure S6). This suggests that the observed cytotoxicity in 4T1 cells is not due to differential nanoparticle cellular uptake but rather to the nanoparticles' specific activity within the tumor microenvironment. Next, the introduction of GSH to GA-DMOS@FeOOH NPs can significantly decrease the cell viability of 3T3 cells (Fig. 3d), confirming that the cytotoxicity of GA-DMOS@FeOOH is closely related to its effect on intracellular GSH levels.

As shown in Fig. 3e, the GSH levels in 4T1 cells treated with GA-DMOS@FeOOH significantly decreased compared with control group, indicating that GA-DMOS@FeOOH could effectively deplete the GSH in tumor cells. The impact of GA-DMOS@FeOOH on GSH levels was also examined using the ThiolTracker Violet GSH probe. Figure 3f shows that GSH levels in 4T1 cells were markedly reduced after incubation with GA-DMOS@FeOOH, while GSH levels in 3T3 cells remained largely unaffected. This differential response can be attributed to the lower basal GSH levels in normal cells, further emphasizing the selectivly GSH depletion capability of GA-DMOS@FeOOH in tumor cells.

To further reflect the GSH depletion ability of the tetrasulfide-bond-containing GA-DMOS@FeOOH NPs, specific probe WSP-5 was used to examine intracellular H_2S production. Figure 3g-h show distinct green fluorescence in cells treated with DMOS@FeOOH NPs,

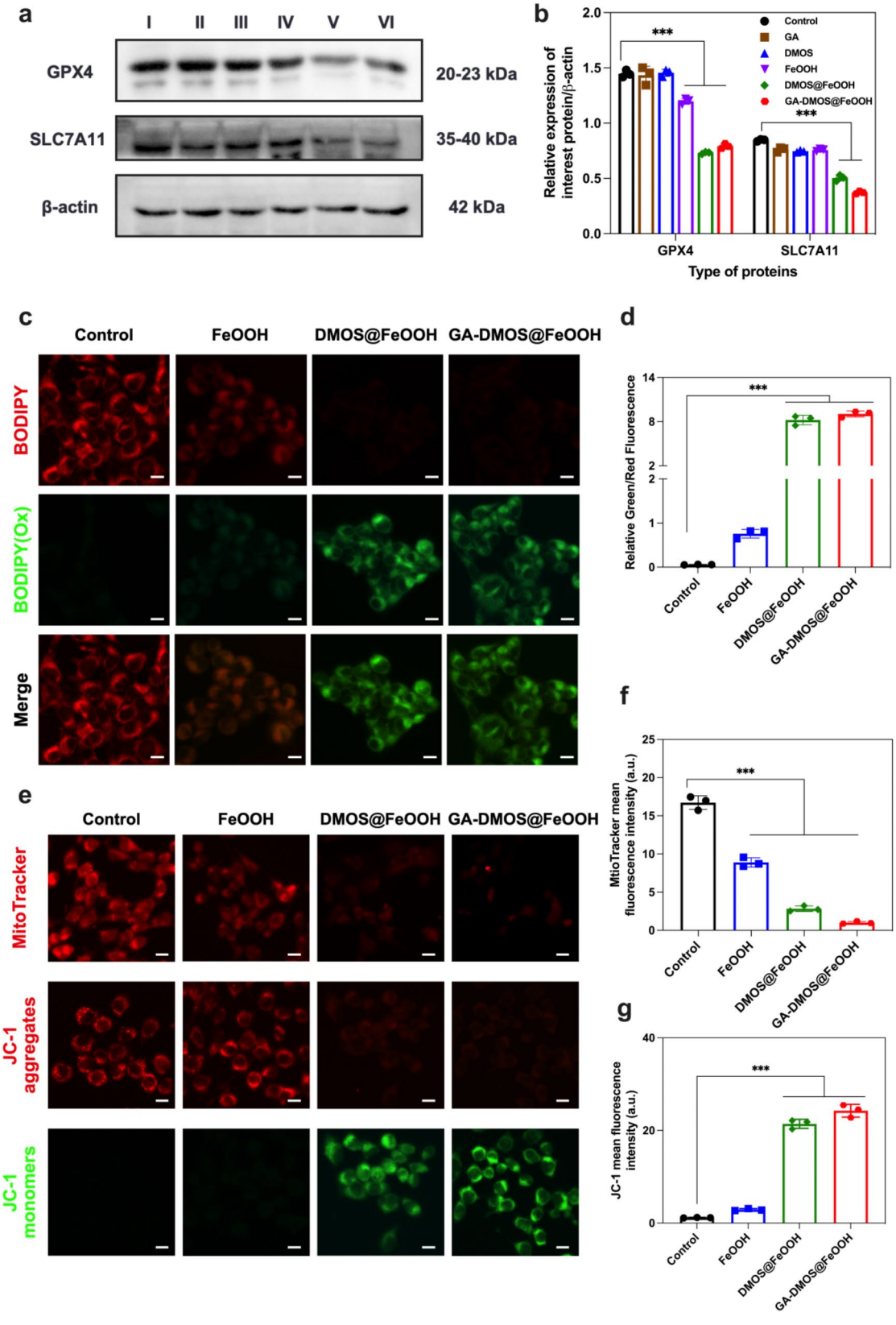

Fig. 4 (See legend on next page.)

(See figure on previous page.)

Fig. 4 In vitro ferroptosis evaluation. (**a**) Western blotting of ferroptosis-related proteins expression levels after different treatments. ((I) Control, (II) GA, (III) DMOS, (IV) FeOOH, (V) DMOS@FeOOH and (VI) GA-DMOS@FeOOH). (**b**) Corresponding quantitative analysis of (a). (**c**-**d**) Lipid peroxides of 4T1 cells stained with BODIPY$^{581/591}$-C11 after incubation with different nanoparticles and quantitative analysis through Image J (scalar bar: 50 μm). (**e**-**g**) Fluorescence images MitoTracker and JC-1 probe to observe mitochondrial membrane potentials for differently treated groups and quantitative analysis (scalar bar: 50 μm)

confirming the production of H_2S. This indicates that the tetrasulfide bonds in GA-DMOS@FeOOH NPs are cleaved upon GSH interaction, releasing H_2S. Next, FeRhoNox-1 probe is employed to prove Fe^{2+} generation. The red fluorescence of FeRhoNox-1 significantly increased in GA-DMOS@FeOOH group, which confirmed the role of GA-DMOS@FeOOH NPs as iron reservoirs (Fig. 3g, i). Finally, intracellular ROS contents were visually observed with DCFH-DA probe, which was visualized through both fluorescent microscopy and FCM. As displayed in Fig. 3g, j, k, a substantial increase in ROS was observed in GA-DMOS@FeOOH group, indicating that the Fe^{2+}-mediated Fenton-like reaction. This massive ROS production further potentiates the cytotoxicity of GA-DMOS@FeOOH, specifically in tumor cells.

Above results provide robust evidence that GA-DMOS@FeOOH NPs exhibit high selectivity toward tumor cells. The nanoparticles effectively deplete intracellular GSH, trigger Fe^{2+} release, and induce a substantial increase in ROS production within the tumor cells, sensitizing them to ferroptosis and resulting in potent tumor cell killing efficacy.

GA-DMOS@FeOOH-induced cell death occurs by ferroptosis

To investigate whether GA-DMOS@FeOOH NPs can effectively induce ferroptosis in 4T1 cells [30], we first performed western blot analysis to quantify key regulatory ferroptosis-associated proteins [31, 32]. Notably, treatment with GA-DMOS@FeOOH led to substantial downregulation of GPX4 and SLC7A11 (Fig. 4a-b), both of which are critical regulators of ferroptosis.

Lipid peroxidation (LPO) accumulation is another hallmark of ferroptosis, representing the degree of oxidation in intracellular lipid structures. The ferroptotic process is characterized by the peroxidation of polyunsaturated fatty acids within cellular membranes, leading to the accumulation of cytotoxic lipid peroxides. BODIPY$^{581/591}$-C11 probe is a well-established fluorescent probe that efficiently labels lipid peroxides [33]. In normal cells, the BODIPY probe retains its inherent red fluorescence. In ferroptotic cells, BODIPY reacts with these lipid peroxides and undergoes oxidation, then converts to BODIPY(Ox), causing a shift in the fluorescence emission to green (around 510 nm). As demonstrated in Fig. 4c-d, **4T1** cells treated with GA-DMOS@FeOOH displayed the most intense green fluorescence and the faintest red fluorescence, indicating robust LPO accumulation in 4T1 cells and oxidative stress triggered by GA-DMOS@FeOOH.

In addition, mitochondrial dysfunction is a well-established feature of ferroptosis [34, 35]. The mitochondrial integrity was examined using MitoTracker Red and JC-1 assays, which are sensitive indicators of mitochondrial membrane potential [36]. As depicted in Fig. 4e-f, the GA-DMOS@FeOOH-treated group exhibited significantly weaker red fluorescence, indicating substantial mitochondrial damage. Moreover, JC-1 is a widely used fluorescent probe for assessing mitochondrial membrane potential. In healthy mitochondria, JC-1 exists as aggregates (dimer form), emitting red fluorescence. During ferroptosis, induced by iron accumulation and oxidative stress, mitochondrial membrane potential disrupted and then JC-1 dissociates into monomers, which emit green fluorescence. Therefore, the JC-1 aggregate/monomer ratio serves as a sensitive marker for mitochondrial damage and ferroptotic activity. In Fig. 4e and g, **4T1** cells treated with GA-DMOS@FeOOH displayed enhanced green fluorescence and decreased red fluorescence, accompanied with the highest JC-1 aggregate/monomer ratio, further suggesting a disruption of the mitochondrial membrane potential and confirming the induction of ferroptosis. Above results provide strong evidence that GA-DMOS@FeOOH induces cell death via ferroptosis, characterized by the depletion of ferroptosis-related proteins, accumulation of LPO, and mitochondrial membrane potential disruption.

Ferroptosis in antitumor therapy of GA-DMOS@FeOOH NPs in vivo

Building on the potent induction of ferroptosis observed in vitro, we next investigated whether GA-DMOS@FeOOH NPs could exert similar antitumor effects in vivo. The antitumor efficacy was evaluated by intravenous administration of GA-DMOS@FeOOH in 4T1 mammary tumor mice. Once the initial tumor volume reached approximately 50 mm^3, the mice were randomly assigned to four groups: Control, FeOOH, DMOS@FeOOH, and GA-DMOS@FeOOH NPs. The process of tumor induction and drug administration were illustrated in Fig. 5a. No substantial inhibition of tumor growth was observed in DMOS@FeOOH group, suggesting that the induction of ferroptosis alone was insufficient to elicit a strong antitumor response. In contrast, GA-DMOS@FeOOH group demonstrated a remarkable suppressive effect on tumor progression, with this group exhibiting the minimal

tumor size and the most pronounced tumor suppression rate compared to the others (Fig. 5b-c). Survival analysis further supported the effectiveness of GA-DMOS@FeOOH, as 50% of the treated mice survived for more than 70 days (Fig. 5d).

To further evaluate the impact of GA-DMOS@FeOOH on tumor progression, immunohistochemical staining of tumor tissues was performed. KI67 staining indicated a substantial reduction in tumor cell proliferation and extensive cell death following GA-DMOS@FeOOH treatment (Fig. 5e-f). Additionally, TUNEL staining showed intense green fluorescence signals in tumor sections from GA-DMOS@FeOOH-treated groups, confirming significant apoptosis and potent suppression of tumor cell proliferation in vivo (Fig. 5e, g).

To evaluate the role of GA-DMOS@FeOOH NPs in inducing ferroptosis in tumor cells, we also analyzed the GSH levels in animal tumors after treatment with different nanoparticles. As illustrated in Fig. 5h, the GA-DMOS@FeOOH group exhibited a marked decline in GSH levels. This depletion of GSH implies that GA-DMOS@FeOOH could trigger ferroptosis by reducing the intracellular antioxidant GSH, thereby enhancing oxidative stress and leading to ferroptotic cell death. Subsequently, tumor sections were stained with reactive oxygen species detection kit, aimed to determine whether GA-DMOS@FeOOH effectively induce ROS generation, thereby facilitating ferroptosis. Figure 5i-j revealed a notable rise in red fluorescence intensity in tumor sections treated with GA-DMOS@FeOOH, suggesting that GA-DMOS@FeOOH are capable of inducing ROS accumulation within tumor cells, which may contribute to ferroptosis induction. Moreover, histological analyses revealed that GPX4 and SLC7A11 levels were significantly reduced, while LPO accumulation was markedly enhanced at the tumor injury sites, providing further evidence that GA-DMOS@FeOOH treatment induced ferroptosis in vivo (Fig. 5k-m). Collectively, these results highlight the potent antitumor efficacy of GA-DMOS@FeOOH NPs in vivo, establishing ferroptosis induction as a pivotal mechanism underlying tumor growth inhibition.

Ferroptosis combined with HMGB1 blockade triggers immune activation

To elucidate the involvement of HMGB1 release in ferroptotic signaling pathways [37, 38], we conducted immunofluorescence assays combined with ELISA quantification to assess intracellular and extracellular HMGB1 levels in 4T1 cells following different nanoparticles (Fig. 6a, c). Our findings showed that DMOS@FeOOH treatment induced significant nuclear-to-cytoplasmic translocation of HMGB1, verifying that ferroptosis can initiate HMGB1 release. In contrast, GA-DMOS@FeOOH treatment resulted in a decrease in HMGB1 secretion and also inhibiting its overall expression. These results were corroborated by immunofluorescent staining of HMGB1 in tumor sections (Fig. 6b, d), which showed similar patterns to those observed in vitro, highlighting the tumor suppressing role of HMGB1 blockade on ferroptosis induction.

Several studies have demonstrated that HMGB1, as an important damage-associated molecular pattern (DAMP), mediates immune responses and activates signaling pathways that promote the infiltration of PMN-MDSCs into the tumor microenvironment through interacting with receptors such as TLR4 (Toll-like receptor 4) and RAGE (Receptor for Advanced Glycation Endproducts) [12]. The release of HMGB1 plays a pivotal role in the tumor microenvironment, promoting the production of chemotactic factors and cytokines, such as CXCL8, MMP-9, IL-10 and TGF-β, which enhance PMN-MDSCs migration into the tumor site and suppress T-cell responses, further amplifying the immunosuppressive microenvironment [39]. Moreover, HMGB1 also promotes MDSC survival through autophagy induction, further contributing to tumor progression [40].

Therefore, we next explored the immune response induced by ferroptosis. Flow cytometric analysis was performed to examine the infiltration of MDSCs, T lymphocytes and dendritic cells [41], as these are key markers of immune response following ferroptosis induction. Flow cytometric gating strategies were outlined in Figure S7. Figure 6e, g shows enhanced infiltration of Gr-1$^+$ myeloid cells into the 4T1 tumor following DMOS@FeOOH treatment, suggesting that ferroptosis may induce immunosuppression by stimulating MDSCs recruitment. Moreover, we observed that PMN-MDSCs exhibited heightened immunosuppressive activity upon treatment with DMOS@FeOOH (Fig. 6e, h). In contrast, GA-DMOS@FeOOH treatment led to a significant diminution of granulocytic MDSCs, particularly following HMGB1 inhibition. As shown in Fig. 6f, i, both the DMOS@FeOOH and GA-DMOS@FeOOH groups exhibited a significant upsurge in CD8$^+$ T cell populations. Furthermore, in the GA-DMOS@FeOOH group, CD8$^+$ T cells exhibited a higher activation state, as indicated by significantly elevated expression of IFN-γ (Figure S8a). These results suggest that GA-DMOS@FeOOH nanoparticles, by inducing ferroptosis in tumor cells and combining with HMGB1 blockade, can activate tumor infiltrating T lymphocytes and potentially inhibit tumor immune escape. Additionally, we also analyzed changes in dendritic cells. The GA-DMOS@FeOOH group displayed the most abundant dendritic cells infiltration, indicating that GA-DMOS@FeOOH nanoparticles effectively promote the activation and function of dendritic cells, enhancing antigen presentation and

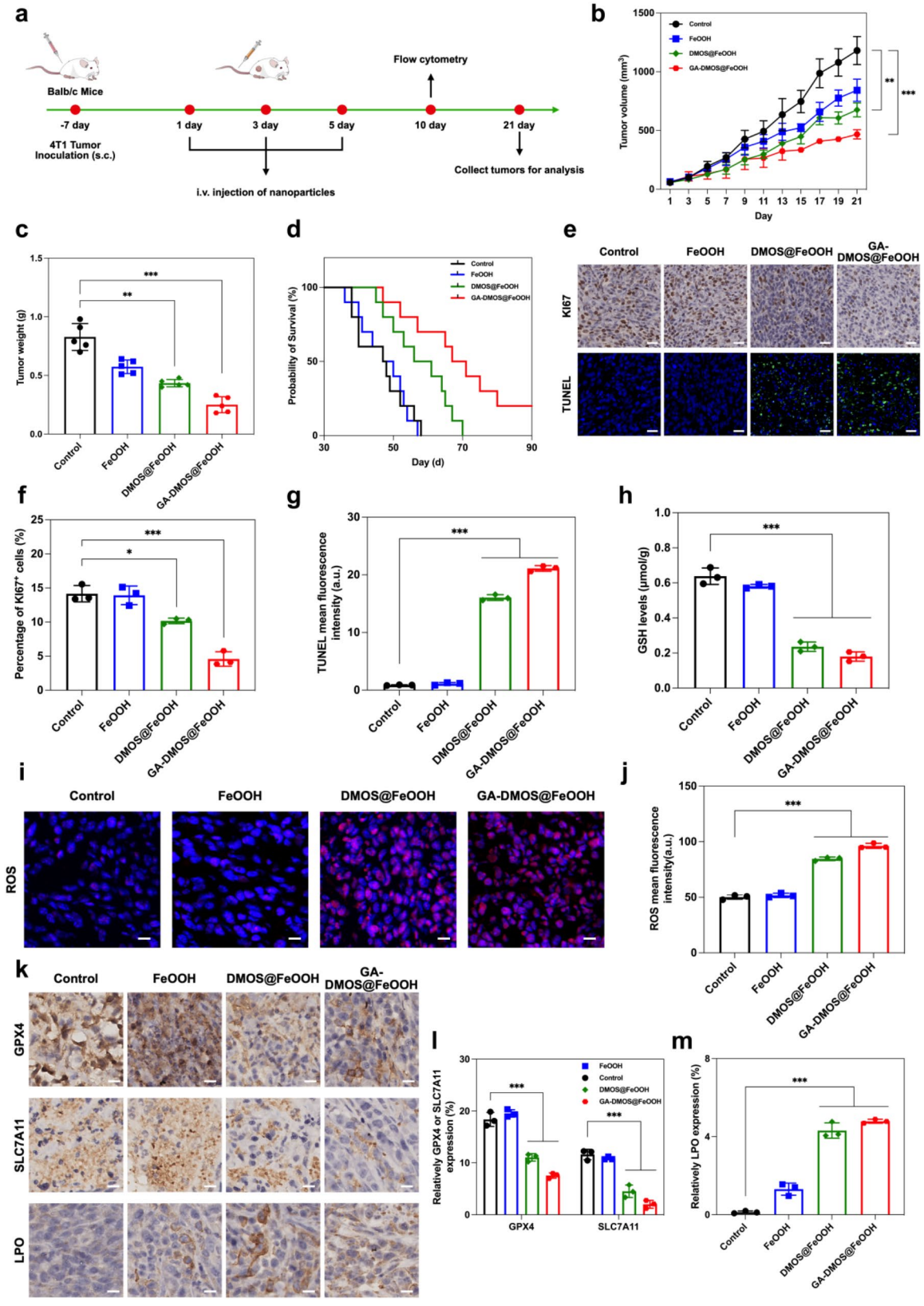

Fig. 5 (See legend on next page.)

(See figure on previous page.)

Fig. 5 In vivo anti-tumor efficacy evaluation. (**a**) Schematic illustration of the animal experimental design for the treatments of differnet nanoparticles in 4T1 tumor-bearing mice. (**b**) Tumor volume curves of mice after different treatments ($n=5$). (**c**) Weights of tumors in mice of each group ($n=5$). (**d**) Survival curves of mice in different treatment groups ($n=10$). (**e**-**g**) KI67 immunohistochemical staining and TUNEL immunofluorescence staining of tumor sections from different groups and quantitative analysis. (**h**) The content of GSH in tumor after different treatments. (**i**) ROS staining of tumor tissue sections from various treatments and (**j**) quantitative analysis. (**k**-**m**) Immunohistochemical staining (GPX4, SLC7A11, LPO) of tumor sections from different groups and quantitative analysis

recognition, thereby further boosting the anti-tumor immune response (Fig. 6f, j).

Next, we assessed cytokines, including IL-10, in the tumors from each group using ELISA. The findings demonstrated a marked decrease in IL-10 levels within tumors after GA-DMOS@FeOOH administration, suggesting that the nanoparticles can modulate the equilibrium of immune factors in tumor microenvironment (Figure S8b), enhance immune activation, and suppress immunosuppressive responses. These findings support the hypothesis that ferroptosis induction combined with HMGB1 blockade may enhance tumor immunotherapy by regulating the immune microenvironment.

To further validate the efficacy of GA-DMOS@FeOOH-mediated ferroptotic immunotherapy, we investigated the combined therapy of GA-DMOS@FeOOH + anti-PD-L1 (aPD-L1) in the 4T1 tumor model [42, 43]. As shown in Fig. 6k-m, the combinatory therapy notably suppressed tumor growth and improved the survival rate. Despite the combined therapy demonstrated a notable suppression of tumor progression, the mice survival rate declined to 50%. We believe this decline may be related to the complexity of the tumor microenvironment and immune evasion mechanisms. Additionally, the effects of ICB immunotherapy require a certain amount of time to fully manifest, and some mice may not have fully controlled tumor growth due to immune tolerance or tumor cell heterogeneity. Additionally, immunofluorescence staining of tumor sections revealed a marked downregulation of GPX4 and SLC7A11 expression and an enhancement of LPO production (Figure S10), further confirming that GA-DMOS@FeOOH-induced ferroptosis sensitizes tumors to checkpoint inhibition. Above data underscore highlight the combined effect of ferroptosis induction and HMGB1 inhibition as a promising approach to boost immunotherapy effectiveness by eliciting a strong anti-tumor immune response.

In vivo biosafety evaluation of GA-DMOS@FeOOH NPs

To assess the potential clinical applicability of GA-DMOS@FeOOH nanoparticles, we conducted a comprehensive in vivo biosafety evaluation. The first step involved hemolysis testing to assess the hemocompatibility of the nanoparticles. As shown in Fig. 7a, GA-DMOS@FeOOH demonstrated a low hemolysis rate (< 5%) even at high concentrations (1000 μg mL^{-1}), indicating their superior hemo-compatibility. Subsequently, Balb/c mice were intravenously injected with GA-DMOS@FeOOH NPs at three time intervals (7, 14, 21 days), with saline serving as the control. At terminal, the mice were euthanized, blood samples and major organs were harvested for further analysis. As depicted in Fig. 7b, no significant differences were observed in the routine blood parameters or biochemical markers between the GA-DMOS@FeOOH-treated mice and the control group, suggesting that GA-DMOS@FeOOH does not adversely affect normal blood or liver function. H&E staining was then performed on the major organs for histological examination. The H&E results (Fig. 7c) showed no signs of acute toxicity in either the control or GA-DMOS@FeOOH-treated groups, suggesting that the nanoparticles do not induce significant tissue damage. Additionally, there were no noticeable differences in the body weights of mice across all groups during the therapeutic period (Figure S11), further supporting the safety of GA-DMOS@FeOOH.

The low toxicity and biocompatibility of such metal species-encapsulated mesoporous silica nanoparticles can be supported by multiple studies [44, 45]. Wang et al. reported an iron-engineered mesoporous silica nanocatalyst and evaluated the in vivo chronic (30 days) and acute (24 h) biocompatibility of this nanocatalyst on healthy Kunming mice, resulting in biosafety in both periods [46]. Moreover, clinical trials involving mesoporous silica have demonstrated the safety and good tolerability of silica in human subjects. Clinical trials (NCT01270139) of silica-gold nanoparticles for photothermal therapy showed no systemic toxicity or organ dysfunction [47]. In brief, these findings demonstrate the exceptional biocompatibility of GA-DMOS@FeOOH nanoparticles, highlighting their potential for safe clinical applications.

Discussion

In this study, we developed an innovative nanoplatform based on FeOOH nanoparticles coated with tetrasulfide bond-doped mesoporous organosilica, which simultaneously carries glycyrrhizic acid. This unique multifunctional nanoplatform was engineered to selectively induce ferroptosis in tumor cells while maintaining minimal toxicity to normal cells, addressing a key challenge in cancer therapy. Since tumor cells often exhibit elevated levels of GSH, which is a critical factor in the pathogenesis of cancer and a hallmark of many malignant cells. This makes GSH a perfect trigger for our nanoplatform, which

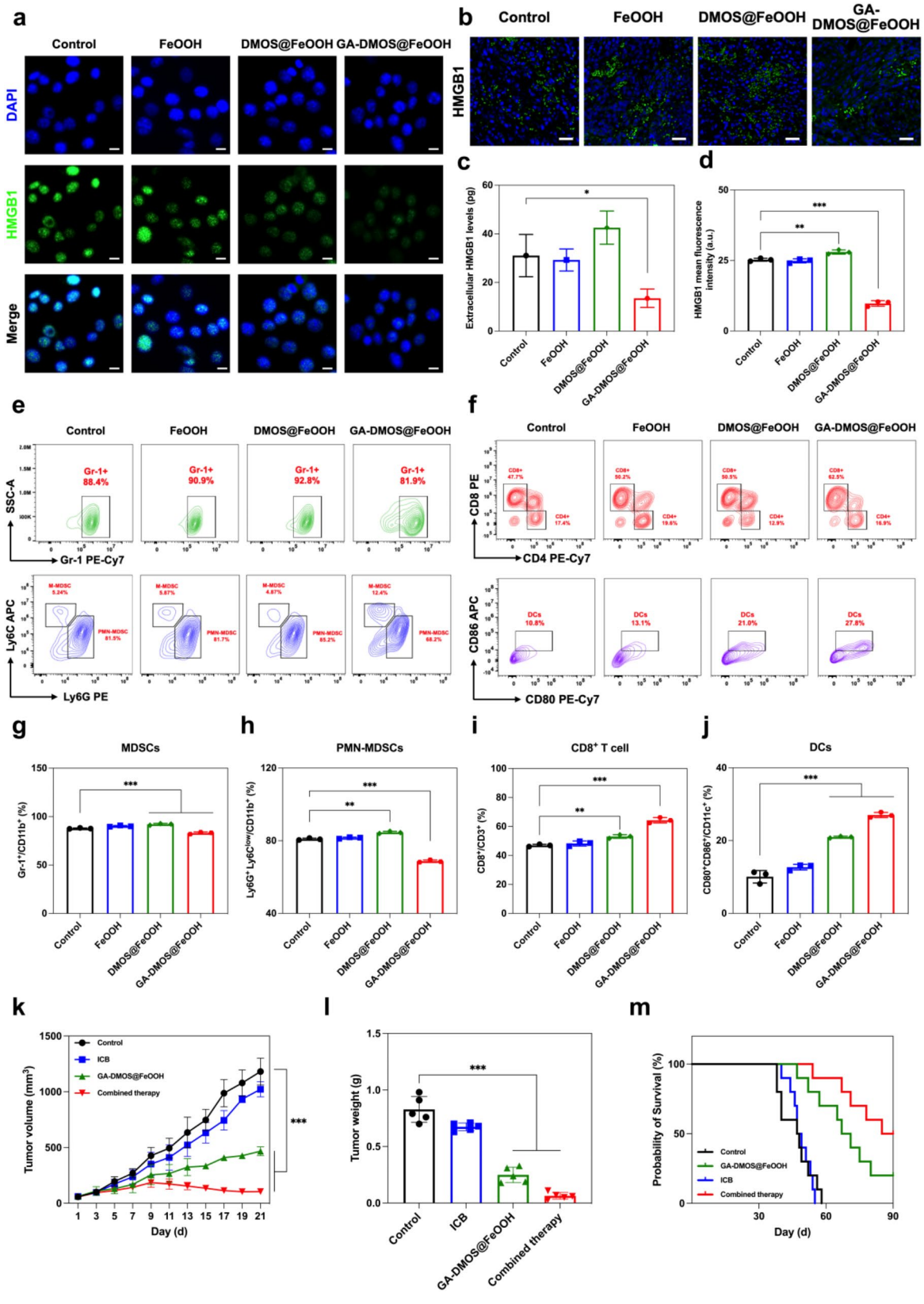

Fig. 6 (See legend on next page.)

(See figure on previous page.)

Fig. 6 In vivo immune activation and exertion of potent antitumor efficacy in combination with an immune checkpoint blockade. (**a**) Immunofluorescence images of nucleus HMGB1 distribution in 4T1 cells under different treatments (scalar bar: 50 μm). (**b**) HMGB1 immunofluorescence staining of tumor sections from different groups and (**d**) quantitative analysis. (**c**) ELISA result of HMGB1 release from 4T1 cells after treating with different nanoformulations. (**e**-**j**) The flow cytometry analysis of MDSCs, PMN-MDSCs, $CD8^+$ T cell and DCs expression in tumor after different treatments ($n = 3$). (**k**) Tumor growth curves ($n = 5$), (**l**) Weights of tumors ($n = 5$) and (**m**) Survival curves of mice in different treatment groups ($n = 10$)

exploits the reductive environment of tumor cells to initiate ferroptosis.

The incorporation of tetrasulfide bonds into the surface coating of the DMOS@FeOOH nanoparticles is a crucial design feature. These bonds are highly sensitive to the elevated levels of GSH found in the tumor microenvironment, leading to the reduction and subsequent cleavage of the tetrasulfide bonds. This cleavage triggers the release of drug-loaded components, including the induction of ferroptosis through the accumulation of lipid peroxides and the participation of iron ions. By depleting intracellular GSH, our nanoplatform enhances oxidative stress and disrupts cellular redox homeostasis, leading to tumor cell death.

While ferroptosis effectively eliminates tumor cells, it also induces the release of HMGB1, a nuclear protein that plays a pivotal role in the immune response. HMGB1 can function as an alarmin, signaling to the immune system that tissue damage has occurred. However, its release in the tumor microenvironment has been shown to contribute to immune evasion and promote the infiltration of MDSCs. These MDSCs suppress T cell-mediated immunity and contribute to the establishment of an immunosuppressive microenvironment, thereby facilitating tumor progression and immune escape. This creates a paradox where while ferroptosis kills tumor cells, it simultaneously exacerbates the immunosuppressive environment, undermining the therapeutic efficacy.

To counteract this, we incorporated glycyrrhizic acid into the nanoplatform. Glycyrrhizic acid, a well-known inhibitor of HMGB1, plays a dual role in mitigating the immunosuppressive effects of ferroptosis. It effectively reduces HMGB1 secretion, thereby preventing the infiltration of MDSCs and restoring T cell function. Moreover, GA possesses anti-inflammatory and immune-modulatory properties, which could enhance the overall anti-tumor immune response. By simultaneously inducing ferroptosis and modulating the immune microenvironment, this nanoplatform presents a promising strategy to overcome tumor immune evasion and improve the therapeutic outcome of ferroptosis-based cancer therapies.

A further advantage of our nanoplatform is its potential synergy with ICB therapy. ICB therapy, which works by reversing T cell exhaustion and blocking immune inhibitory pathways (PD-1/PD-L1), has shown tremendous promise in cancer immunotherapy. However, the immunosuppressive tumor microenvironment, particularly the presence of MDSCs and regulatory T cells, limits the effectiveness of ICB therapy. By integrating ferroptosis induction with GA-mediated inhibition of MDSCs infiltration, our nanoplatform enhances the efficacy of ICB therapy, boosting T lymphocyte anti-tumor activity. This combination could offer a more potent therapeutic strategy, addressing both the intrinsic tumor cell death mechanisms and the modulation of the tumor immune microenvironment.

Our results from in vitro and in vivo experiments further support the promise of this nanoplatform. In tumor-bearing mouse models, the nanoplatform demonstrated selective accumulation at the tumor site, where it induced ferroptosis in tumor cells while minimizing systemic toxicity. Importantly, there was no significant damage to normal tissues, suggesting that the platform has a favorable safety profile. This high selectivity is crucial for clinical applications, as it minimizes off-target effects and enhances the overall therapeutic index.

Despite the promising outcomes, several challenges remain that must be addressed to fully realize the potential of this therapeutic approach. The precise control of nanoparticle size, surface charge, and drug release kinetics is critical for optimizing the platform's therapeutic efficacy. Small variations in these parameters can significantly affect the distribution, uptake, and release profile of the drug, ultimately influencing its therapeutic outcome. Therefore, refining these aspects through more advanced fabrication techniques and careful parameter tuning will be necessary for enhancing the overall performance of the nanoplatform.

Furthermore, while our approach demonstrates potential in reducing the infiltration of MDSCs and improving T cell responses, the tumor immune microenvironment remains highly complex and multifactorial, necessitating further exploration. The immune landscape within tumors can vary greatly depending on several factors, such as tumor type, stage, and genetic heterogeneity. These variables may impact not only the effectiveness of immune modulation strategies but also the ability of the nanoplatform to consistently target and modify the tumor environment. Moreover, tumors often exhibit significant heterogeneity. Therefore, the effects of this nanoplatform could be markedly different across different cancer types, which further underscores the need for comprehensive studies to better understand these interactions. In light of these complexities, additional studies are required to systematically evaluate the nanoplatform's

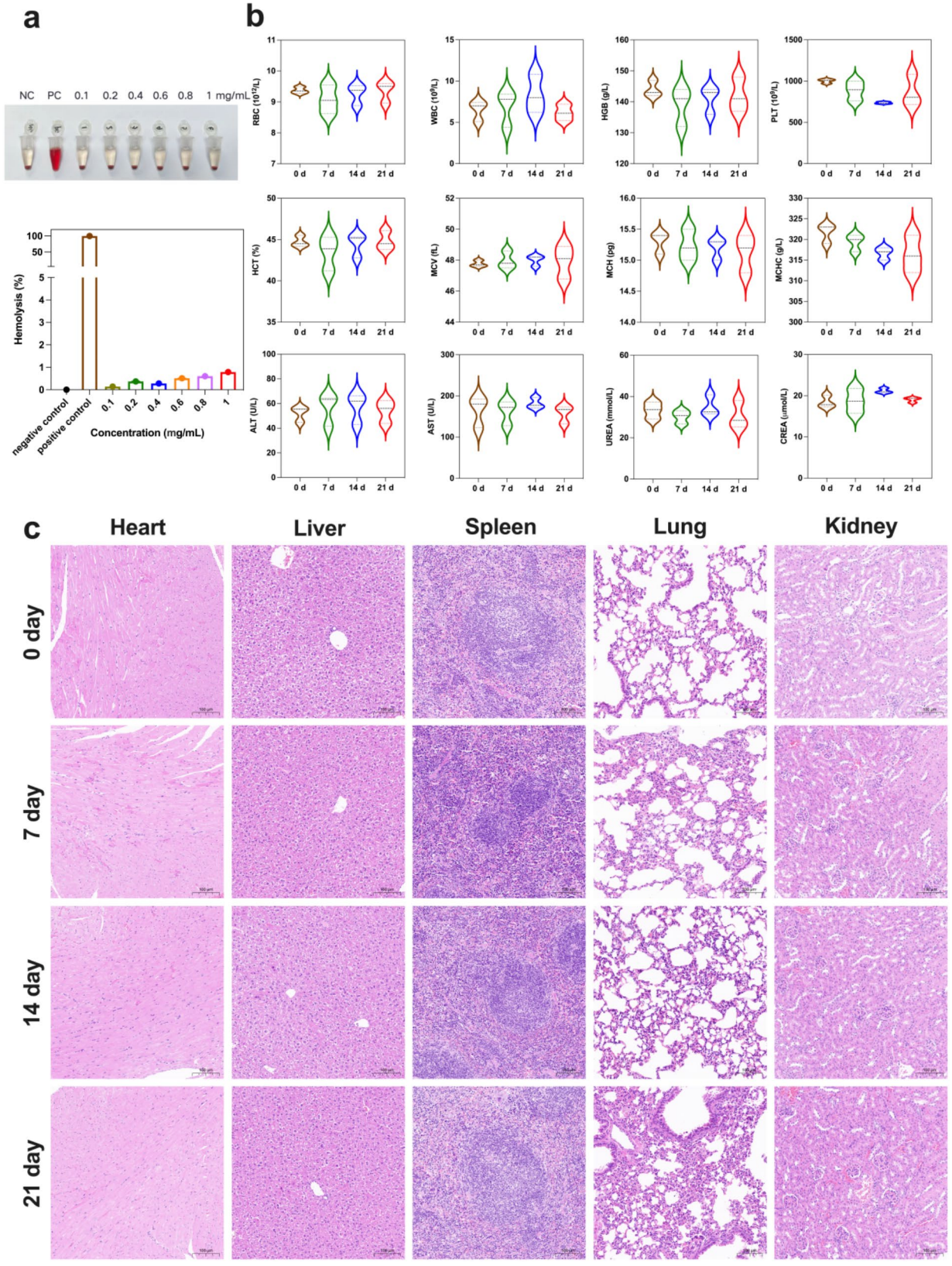

Fig. 7 The biocompatibility of GA-DMOS@FeOOH NPs. (**a**) Hemolysis rate of GA-DMOS@FeOOH with different concentrations, with DI water as the positive control and saline as the negative control. (**b**) Blood parameters and blood biochemical indices of balb/c mice at different time points ($n = 3$). (**c**) H&E staining of various organs (heart, liver, spleen, lung and kidney) at different time points

performance across different tumor types, immune environments, and therapeutic settings. These investigations will help to refine the platform's design, optimize its therapeutic efficacy, and ensure its applicability in clinical practice.

In summary, the GA-DMOS@FeOOH nanoplatform presented in this study induces ferroptosis in tumor cells by exploiting the high GSH environment, while concurrently utilizing glycyrrhizic acid to inhibit HMGB1 release and reduce the infiltration of immunosuppressive cells. Additionally, when combined with immune checkpoint blockade therapy, the nanoplatform significantly enhances anti-tumor immune responses. This strategy not only offers a novel approach for cancer immunotherapy but also opens new avenues for the clinical application of immunotherapy. With further optimization of the nanoplatform design and therapeutic efficacy evaluation, we believe that this platform has the potential to become a clinically viable strategy for cancer immunotherapy.

Conclusion

In this work, we successfully developed a GSH-triggered nanoplatform, GA-DMOS@FeOOH, for selectively inducing ferroptosis in cancer cells and eliciting an anti-tumor immune response. As the tetrasulfide bond-modified GA-DMOS@FeOOH are sensitive to reductive environments, this nanoplatform could deplete intracellular GSH and release Fe^{2+}, which then triggers ferroptosis in cancer cells, while sparing immune cells. Concurrently, the GSH-responsive GA release was coupled with GSH depletion, which effectively prevented MDSCs infiltration through inhibiting HMGB1 release. This, in turn, reverses the immunosuppressive tumor microenvironment typically induced by ferroptosis. The combined effects of ferroptosis induction and HMGB1 blockade synergistically activate potent anti-tumor immune responses. Notably, this two-pronged approach renders 4T1 mammary tumors more sensitive to immune checkpoint blockade, enhancing the overall therapeutic efficacy. Overall, our findings provide valuable insights into the development of immune-modulating anticancer therapies, presenting a promising approach to address the challenges of cancer immunotherapy and enhance cancer treatment.

Supplementary Information

The online version contains supplementary material available at https://doi.org/10.1186/s12951-025-03307-z.

Supplementary Material 1

Acknowledgements
We would like to thank the Core Facility of the First Affiliated Hospital of Nanjing Medical University for its help in the experiment.

Author contributions
Xuan Sha, Chuanbing Wang and Yang Liu: Project administration, Writing–original draft, Visualization, Methodology, Investigation. Nan Zhong and Yishi Lu: Writing – review & editing, Methodology, Data curation, Visualization. Qi Zhang, Shangyu Lu, and Doudou He: Validation, Methodology. Jingying Jin: Writing – review & editing, Conceptualization, Supervision. Yuxia Tang and Shouju Wang: Resources, Funding acquisition, Writing – review & editing, Conceptualization, Supervision. All authors reviewed the manuscript.

Funding
This work was supported by the National Natural Science Foundation of China (No. 82372019), Double First Class Foundation of China Pharmaceutical University (No. CPUQNJC22_03) and China Postdoctoral Science Foundation (Grant No. 2021TQ0158, 2022M711678).

Data availability
No datasets were generated or analysed during the current study.

Declarations

Ethics approval and consent to participate
In vivo studies were conducted using protocols reviewed and approved by the Institutional Animal Care and Use Committee of Nanjing Medical University (approval number: 2310051).

Consent for publication
All authors are consent for publication.

Competing interests
The authors declare no competing interests.

Author details
[1]Laboratory of Molecular Imaging, Department of Radiology, The First Affiliated Hospital with Nanjing Medical University, Nanjing, China
[2]Department of Ultrasound, The First Affiliated Hospital with Nanjing Medical University, Nanjing, China
[3]Department of Interventional Radiology, The First Affiliated Hospital with Nanjing Medical University, Nanjing, China

Received: 27 February 2025 / Accepted: 8 March 2025
Published online: 19 March 2025

References

1. Shi Junxiao Z, Zhichao Y, Haozan, et al. RNA m6A modification in ferroptosis: implications for advancing tumor immunotherapy. Mol Cancer. 2024;23(1):213.
2. Guang L, Li Z, Boyi G. The roles of ferroptosis in cancer: tumor suppression, tumor microenvironment, and therapeutic interventions. Cancer Cell. 2024;42(4):513–34.
3. Zheng Yichen S, Lingqi G, Jiamin, et al. The crosstalk between ferroptosis and anti-tumor immunity in the tumor microenvironment: molecular mechanisms and therapeutic controversy. Cancer Commun. 2023;43(10):1071–96.
4. Ning Shipeng S, Ping Z, Xinyan, et al. Pyridinium rotor strategy toward a robust photothermal agent for STING activation and multimodal image-guided immunotherapy for triple-negative breast cancer. J Am Chem Soc. 2025;147(9):7433–44.
5. Zhou Qian M, Daishi YL, et al. Ferroptosis in cancer: from molecular mechanisms to therapeutic strategies. Signal Transduct Target Therapy. 2024;9(1):55.
6. Yang Huocheng Y, Xuemei L, Yingqi, et al. Ferroptosis nanomedicine: clinical challenges and opportunities for modulating tumor metabolic and immunological landscape. ACS Nano. 2023;17(16):15328–53.
7. Dai Yeneng G, Ziang L, Dongliang, et al. Metal-coordinated NIR-II nanoadjuvants with nanobody conjugation for potentiating immunotherapy by tumor metabolism reprogramming. Adv Sci. 2024;11(34):e2404886.
8. Dai Xiaomeng Z, Jia B, Xuanwen, et al. Induction of tumor ferroptosis-dependent immunity via an injectable attractive pickering emulsion gel. Adv Mater. 2023;35(35):e2303542.

9. Chen Congcong Y, Yabing G, Yanguan, et al. CYP1B1 inhibits ferroptosis and induces anti-PD-1 resistance by degrading ACSL4 in colorectal cancer. Cell Death Dis. 2023;14(4):271.
10. Chen Xin K, Rui K, Guido, et al. Broadening horizons: the role of ferroptosis in cancer. Nat Reviews Clin Oncol. 2021;18(5):280–96.
11. Chen Ruochan K, Rui, Tang Daolin. The mechanism of HMGB1 secretion and release. Experimental Mol Med. 2022;54(2):91–102.
12. Özbay KF, Gül C, Beatrice-Ana B, Bianca M et al. S100A9 and HMGB1 orchestrate MDSC-mediated immunosuppression in melanoma through TLR4 signaling. J Immunother Cancer. 2024;12(9).
13. Conche Claire F, Fabian Pešić, Marina, et al. Combining ferroptosis induction with MDSC blockade renders primary tumours and metastases in liver sensitive to immune checkpoint blockade. Gut. 2023;72(9):1774–82.
14. Wen Qirong L. The release and activity of HMGB1 in ferroptosis. Biochem Biophys Res Commun. 2019;510(2):278–83.
15. Bell Hannah N, Stockwell Brent R, Zou W. Ironing out the role of ferroptosis in immunity. Immunity. 2024;57(5):941–56.
16. Kim Rina T, Devon V, Robert H, et al. Ferroptosis of immune cells in the tumor microenvironment. Trends Pharmacol Sci. 2023;44(8):542–52.
17. Li Jingbo L, Zhuan JZ, et al. Tumor-specific GPX4 degradation enhances ferroptosis-initiated antitumor immune response in mouse models of pancreatic cancer. Sci Transl Med. 2023;15(720):eadg3049.
18. Huang Yingyu X, Wei A, Samira, et al. Crosstalk between hepatic glutathione efflux and tumor targeting efficiency of indocyanine green-conjugated gold nanoparticles. Angewandte Chemie-International Ed. 2023;62(45):e202308909.
19. Ning Shipeng L, Meng Z, Daoming, et al. Type-I AIE photosensitizer loaded biomimetic system boosting cuproptosis to inhibit breast cancer metastasis and rechallenge. ACS Nano. 2023;17(11):10206–17.
20. Chen Zhongxian L, Zeming Z, Yingguang, et al. Bionic aggregation-induced emission photosensitizer for enhanced cancer immunotherapy. Mater Today Bio. 2024;28:101217.
21. Zhang Ni P, Wei X, Jingfeng, et al. Biomimetic single-atom nanozyme for dual starvation-enhanced breast cancer immunotherapy. Adv Healthc Mater. 2024:e2401362.
22. Xu Kun, Li K, Ye H, et al. Engineered nanoplatform mediated gas therapy enhanced ferroptosis for tumor therapy in vivo. Bioactive Mater. 2025;44:488–500.
23. Wu Kai Z, Wei C, Hao, et al. An iron oxyhydroxide-based nanosystem sensitizes ferroptosis by a three-pronged strategy in breast cancer stem cells. Acta Biomater. 2023;160:281–96.
24. Liu Bin L, Shuang W, Zhao, et al. A tumor-microenvironment-responsive nanocomposite for hydrogen sulfide gas and trimodal-enhanced enzyme dynamic therapy. Adv Mater. 2021;33(30):e2101223.
25. Liu Shuwei Z, Mengsi J, Hao, et al. Iron-containing protein-mimic supramolecular iron delivery systems for ferroptosis tumor therapy. J AM CHEM SOC. 2023;145(1):160–70.
26. Chen L, Ming H, Li B, et al. Tumor-specific nano-herb delivery system with high L-arginine loading for synergistic chemo and gas therapy against cervical cancer. Small. 2024;20:e2403869.
27. Li L, Yulin X. Biofilm microenvironment-activated multimodal therapy nanoplatform for effective anti-bacterial treatment and wound healing. Acta Biomater. 2024;183:221–34.
28. Niu Shining Q, Pu M, Jialan, et al. Light/glutathione-ignited nanobombs integrating Azo and tetrasulfide bonds for multimodal therapy of colorectal cancer. J Colloid Interf SCI. 2024;659:474–85.
29. Huang Lin Z, Jiaoyang W, Guochao, et al. A strategy of adding fuel to the flames enables a self-accelerating cycle of ferroptosis-cuproptosis for potent antitumor therapy. Biomaterials. 2024;311:122701.
30. Wang He J, Di F, Dexiang, et al. Transformable supramolecular self-assembled peptides for cascade self-enhanced ferroptosis primed cancer immunotherapy. Adv Mater. 2024;36(21):e2311733.
31. Ruizhi H, Chen D, Xinyue D, et al. Topology regulation of nanomedicine for autophagy-augmented ferroptosis and cancer immunotherapy. Sci Bull. 2023;68(1):77–94.
32. Liu Jianping Z, Jiezhao Z, Ye, et al. Ultrathin clay nanoparticles-mediated mutual reinforcement of ferroptosis and cancer immunotherapy. Adv Mater. 2024;36(9):e2309562.
33. Zhang Yiqun Z, Ni X, Jianghao, et al. In situ hydrogel based on Cu-Fe3O4 nanoclusters exploits oxidative stress and the ferroptosis/cuproptosis pathway for chemodynamic therapy. Biomaterials. 2024;311:122675.
34. Yang Jiacai D, Li Y, Luodan, et al. Nanomedicine enables autophagy-enhanced cancer-cell ferroptosis. Sci Bull. 2021;66(5):464–77.
35. Lei Huali L. Manganese molybdate nanodots with dual amplification of STING activation for cycle treatment of metalloimmunotherapy. Bioactive Mater. 2024;31:53–62.
36. Yang Nailin G, Fei L, Bo, et al. Magnesium galvanic cells produce hydrogen and modulate the tumor microenvironment to inhibit cancer growth. Nat Commun. 2022;13(1):2336.
37. Jiang Le K, Ning L, Tongyuan, et al. Ferroptosis as a p53-mediated activity during tumour suppression. Nature. 2015;520(7545):57–62.
38. Zhang Yilei S, Jiejun L, Xiaoguang, et al. BAP1 links metabolic regulation of ferroptosis to tumour suppression. Nat Cell Biol. 2018;20(10):1181–92.
39. Parker Katherine H, Sinha Pratima, Horn Lucas A, et al. HMGB1 enhances immune suppression by facilitating the differentiation and suppressive activity of myeloid-derived suppressor cells. Cancer Res. 2014;74(20):5723–33.
40. Parker Katherine H, Horn Lucas A, Ostrand-Rosenberg, Suzanne. High-mobility group box protein 1 promotes the survival of myeloid-derived suppressor cells by inducing autophagy. J Leukoc Biol. 2016;100(3):463–70.
41. Hubert Pascale R, Patrick D, Stephanie et al. Extracellular HMGB1 blockade inhibits tumor growth through profoundly remodeling immune microenvironment and enhances checkpoint inhibitor-based immunotherapy. J Immunother Cancer. 2021;9(3).
42. Huang Yi G, Zili F, Yang, et al. Inhibition of the adenosinergic pathway: the indispensable part of oncological therapy in the future. Purinergic Signalling. 2019;15(1):53–67.
43. Huang Yi S, Yanbin W, Qingjie, et al. Enzyme responsiveness enhances the specificity and effectiveness of nanoparticles for the treatment of B16F10 melanoma. J Controlled Release. 2019;316:208–22.
44. Xu Bolong L, Rui SS, et al. Multifunctional mesoporous silica nanoparticles for biomedical applications. Signal Transduct Target Therapy. 2023;8(1):435.
45. Araceli L-V, Estepa-Fernández Alejandra, García-Fernández Alba, et al. Biosafety of mesoporous silica nanoparticles; towards clinical translation. Adv Drug Deliv Rev. 2023;201:115049.
46. Wang Liying H, Minfeng C. Iron-engineered mesoporous silica nanocatalyst with biodegradable and catalytic framework for tumor-specific therapy. Biomaterials. 2018;163:1–13.
47. Kharlamov Alexander N, Feinstein John A, Cramer John A, et al. Plasmonic photothermal therapy of atherosclerosis with nanoparticles: long-term outcomes and safety in NANOM-FIM trial. Future Cardiol. 2017;13(4):345–63.

Publisher's note